MACHINE LEARNING
Science and Technology

PAPER

AtOMICS: a deep learning-based automated optomechanical intelligent coupling system for testing and characterization of silicon photonics chiplets

Jaime Gonzalo Flor Flores[1,*], **Jim Solomon**[1], **Connor Nasseraddin**[1], **Talha Yerebakan**[1], **Andrey B Matsko**[2] and **Chee Wei Wong**[1,*]

[1] Fang Lu Mesoscopic Optics and Quantum Electronics Laboratory, University of California, Los Angeles, CA 90095, United States of America
[2] NASA, Jet Propulsion Laboratory (JPL), Pasadena, CA 91109, United States of America
[*] Authors to whom any correspondence should be addressed.

E-mail: jflorflores@ucla.edu and cheewei.wong@ucla.edu

Keywords: optomechanical accelerometer, cavity optomechanics, testing, automatic coupling, active alignment, silicon photonics, neural networks

OPEN ACCESS

RECEIVED
8 October 2024

REVISED
26 December 2024

ACCEPTED FOR PUBLICATION
14 January 2025

PUBLISHED
29 January 2025

Abstract

Recent advances in silicon photonics promise to revolutionize modern technology by improving the performance of everyday devices in multiple fields (Thomson *et al* 2016 *J. Opt.* **18** 073003). However, as the industry moves into a mass fabrication phase, the problem of adequate testing of integrated silicon photonics devices remains to be solved. A cost-efficient manner that reduces schedule risk needs to involve automated testing of multiple devices that share common characteristics such as input–output coupling mechanisms, but at the same time needs to be generalizable to various types of devices and scenarios. This paper presents a neural network-based automated system designed for in-plane fiber-chip-fiber testing, characterization, and active alignment of silicon photonic devices that use process-design-kit library edge couplers. The presented approach combines state-of-the-art computer vision techniques with time-series analysis, to control a testing setup that can process multiple devices and be quickly tuned to incorporate additional hardware. The system can operate at vacuum or atmospheric pressures and maintains stability for fairly long time periods in excess of a month.

1. Introduction

As modern advances push the boundaries of current technologies in search for higher performance devices, silicon photonics is emerging as a disruptive technology that promises to revolutionize multiple areas by introducing technologies such as optical sensing [1–5], quantum photonics [6, 7] and computing [8, 9], chaos-based secure communications [10–12], and photonics neural networks [13, 14]. After decades of research and significant investment, silicon is the mainstream workhorse of the semiconductor industry and its fabrication process is a mature infrastructure, with high process yield and precision nanofabrication. For example, with silicon-on-insulator (SOI) platforms, silicon photonics learns from techniques in silicon complementary metal–oxide semiconductors (CMOS) processes with system commercialization and foundry processes [15–18].

With the growth of silicon photonics commercialization and foundries, new challenges in packaging and testing should be addressed to fully integrate the technology. While the cost of packaging for traditional integrated circuits is variable, the most significant cost reductions come from optimizations in the process, which achieve high throughput [19]; this includes the selection of appropriate processes that can be automated. In the case of testing, prices vary from a flat rate of 2% of the total manufacturing cost up to an order-of-magnitude higher [20], depending on the amount of wor performed and the reductions in liability cost that it could provide. However, packing and testing photonic devices is usually more expensive because the low bandgap of silicon requires that the light signal necessary to drive the system comes from an external

source [21]. When the light source is not built directly onto the silicon photonics chip (e.g. through heterogeneous integration), optical components need to be aligned to couple the light source. There are three main options to couple an external light source to a silicon photonics chip. The first is by grating couplers, which couple a fiber/fiber-array positioned on top of the structure, providing good alignment tolerance on the order of a few micrometers. However, grating couplers usually have a large footprint ($\approx$100 μm^2) and higher insertion losses than other methods. The second method is evanescent coupling, where an inverse coupler is needed in close proximity to the input waveguide, which has been demonstrated by using polymer waveguides [22]. The third method is edge coupling, where a lensed optical fiber [23–25] can be positioned on the side of the chip and coupled to an inverse tapered coupler used for mode matching. A lensed fiber for a laser wavelength of around 1550 nm can produce a spot size down to $\approx$2 μm and a $\approx$12 μm Gaussian waist for this type of coupling; the mode converter couples this mode from the fiber to the waveguide. This method does not use a large die area, and usually provides the highest input power [26]. Other novel coupling techniques that include subwavelength-gratings [27, 28] or light in-coupling to fiber via imprinted nanostructures on fibers [29], represent variations of the described processes. However, silicon photonics using CMOS processes needs to adhere to technological constraints [30]. One of the main design rules concerns the dimension requirements for the waveguides and couplers; in fact, the thickness of the waveguide is usually fixed and needs to be matched to the top membrane of the SOI wafer being used, usually 220–250 nm [15]. Under these dimensional constraints, the alignment tolerances needed for this process are typically sub-micron, as will be described shortly.

Multiple techniques have been suggested to improve the edge coupling process, including improvements to the couplers [31, 32] and the placement of the fibers [26]. The high throughput required to produce thousands of devices at a reduced cost can be further improved with automated packaging and testing processes [33–35]. In this paper we present an '*AuTomated Opto-Mechanical Intelligent Coupling System*' (AtOMICS), which combines testing hardware control, state-of-the-art computer vision algorithms, and customized time-series analysis models in order to generate a setup suitable for testing and characterization of silicon photonics chiplets and that can also be used for active alignment during the packaging process of laser-detector coupled devices. By replacing actuator drivers or adding additional data acquisition devices, AtOMICS is a flexible program that is readily compatible with other hardware too. While the computer vision models used in AtOMICS have been optimized to detect the inverse couplers and optical fibers, which we present in the following study, no constraints on magnification or specific patterns included in the testing chiplets have been used on the computer vision models. As a result, the software can be readily generalized to multiple formats of chip input–output coupling without major changes.

In the following sections, first we illustrate the system and its hardware, including the integrated data acquisition equipment. Second, we describe the system's algorithms. Third we detail the system performance data for the coupling process, long-term measurement, and coupling stability, with the latter having a potential application in active alignment during packaging processes.

2. AtOMICS description

2.1. Hardware and physical connections

The components of AtOMICS are shown in figure 1(a). The system is designed to couple input and output optical fibers at the edges of a silicon photonics chiplet, with sub-micrometer alignment tolerances. Implemented inside a Janis ST-500 vacuum chamber, the system can operate at ambient pressure or vacuum, enabling the test of both regular silicon photonics devices and low pressure/temperature optical transducers in dual operation. The test results presented in the current paper have been collected in ambient or vacuum at $\approx$30 mTorr, and have been done with pressures as low as $\approx$1 μTorr. Figure 1(b) shows a zoomed-in image of the vacuum chamber and the internal components of the setup. The center gold stage is the chiplet mount, which includes a temperature controller, and is located on top of an x–y piezoelectric positioner and a spacer block. The right and the left towers are a stack of x–y–z positioners that move the input and output optical fibers to couple them to the waveguides on the silicon photonics chiplets. In our case, the piezoelectric stages are a set of two Attocube ANPx101s on the x- and y-axis, and an Attocube ANPz101 on the z-axis. Other stages can be used by replacing the controller driver in the program, as the algorithms and calculations are hardware independent. The entire structure is mounted on a support plate on top of a goniometer with a travel range of 10°. The goniometer is capable of moving the entire setup and is used as a way to input precise gravitational forces and induce changes in acceleration when testing photonic optomechanical sensors [2]. The vacuum chamber is closed by a lid that has a clear visor, and a microscope lens is mounted on top, as shown in figure 1(a). The microscope has three single-axis motors that can move it along the x-, y-, and z-axes, allowing it to reach the entire chiplet and the optical fibers. These motors are controlled by an

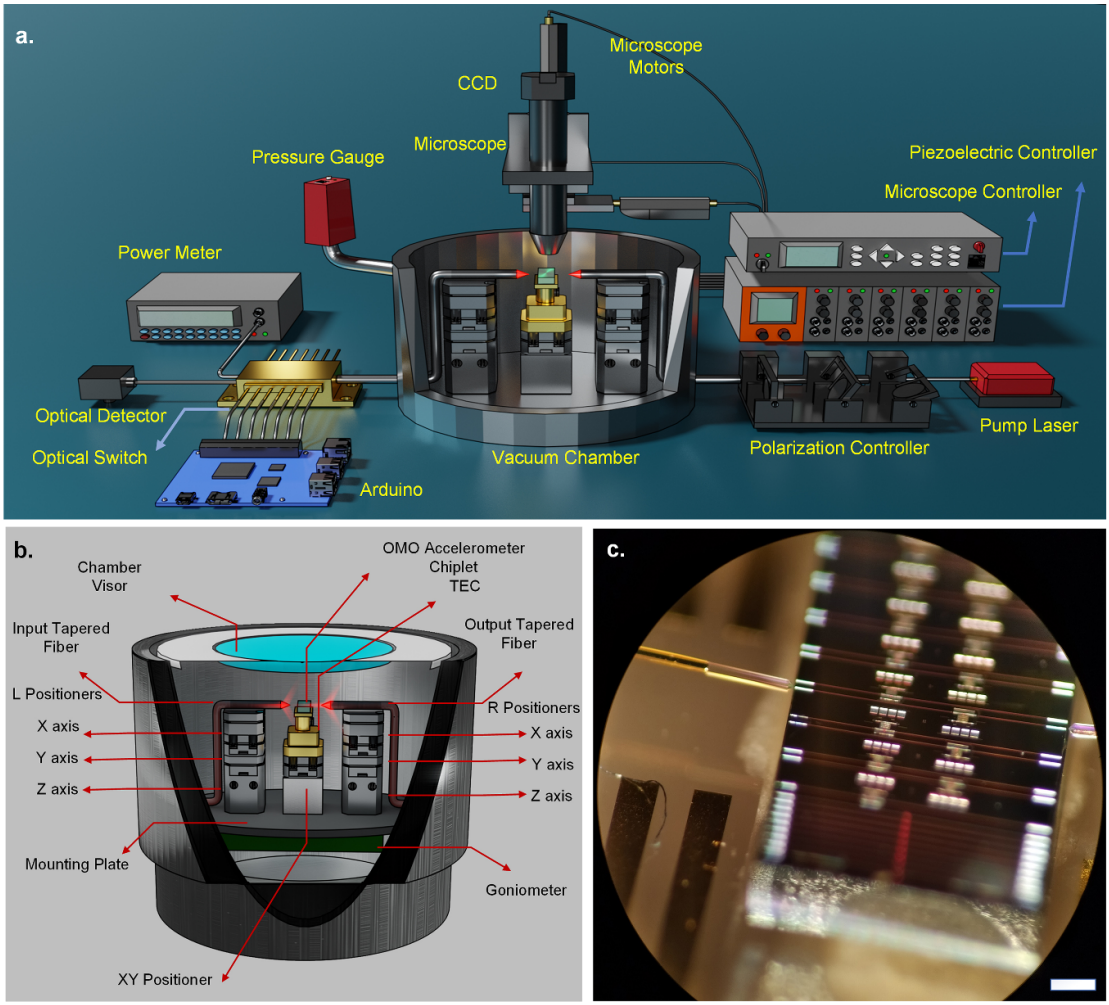

Figure 1. AtOMICS hardware setup and edge coupling. (a) Hardware integrated to AtOMICS. The chiplet is mounted inside the vacuum chamber and is coupled to a pair of lensed fibers. The microscope and CCD cameras monitor the positions of the optical fibers and the inverse tapered couplers. The system integrates a piezoelectric controller that translates the stages inside the chamber and a microscope controller that translates the camera axis. A pump laser and a polarization controller are connected to the input optical fiber, and an optical switch connects the output signal with the power meter and other data acquisition equipment. (b) A zoomed-in depiction of the vacuum chamber interior. Each optical fiber is mounted on a 3-stage tower of piezoelectric stages that translate in the x–y–z axes. The interior setup is assembled on a mounting plate, located on a goniometer to tilt the chiplet assembly. (c) The microscope image of a silicon photonics optomechanical chiplet coupled using the AtOMICS setup. The chiplet is composed of multiple silicon optomechanical transducers arranged into two vertical lines. The lensed optical fiber on the left of the chiplet is aligned to the inverse tapered coupler (in white). The optical waveguide, which goes from the left of the coupler to the silicon photonics optomechanical transducer, is shown in lighter red across the chiplet. Scale bar is 200 μm.

ESP-300 controller and are equipped with relative encoders. The encoders are further tracked by AtOMICS and correlated to the position of the piezoelectric stages.

Figure 2 shows the rest of the elements of the system and how data is transmitted across them. The yellow arrows show the flow of light and experimental data collected in the optical carrier. Control signals are marked in blue and are bidirectional when data is read from the hardware and used as feedback to the software controller; movement confirmation is not taken as a return control signal in this case. The light blue arrows represent a physical input that is sent to the testing device, which could be the application of an external force or a magnetic field. The input side of the vacuum chamber has a lensed optical fiber that is connected to the laser source, which provides the optical excitation for the photonics devices and is fed into a motorized polarization controller. The output fiber is connected to an optical switch, which is driven by an Arduino and connects via a universal asynchronous receiver/transmitter. The optical switch sends the output optical signal to an external power meter that monitors the changes inside the vacuum chamber and provides a feedback signal to trigger the coupling controller. When the system is coupled and the power is stable, the switch sends the output signal to an optical detector that is connected to the data acquisition hardware; some examples of hardware supported by AtOMICS for data collection are oscilloscopes, frequency counters, spectrum analyzers, and multipurpose data acquisition hardware. The collected data from these instruments

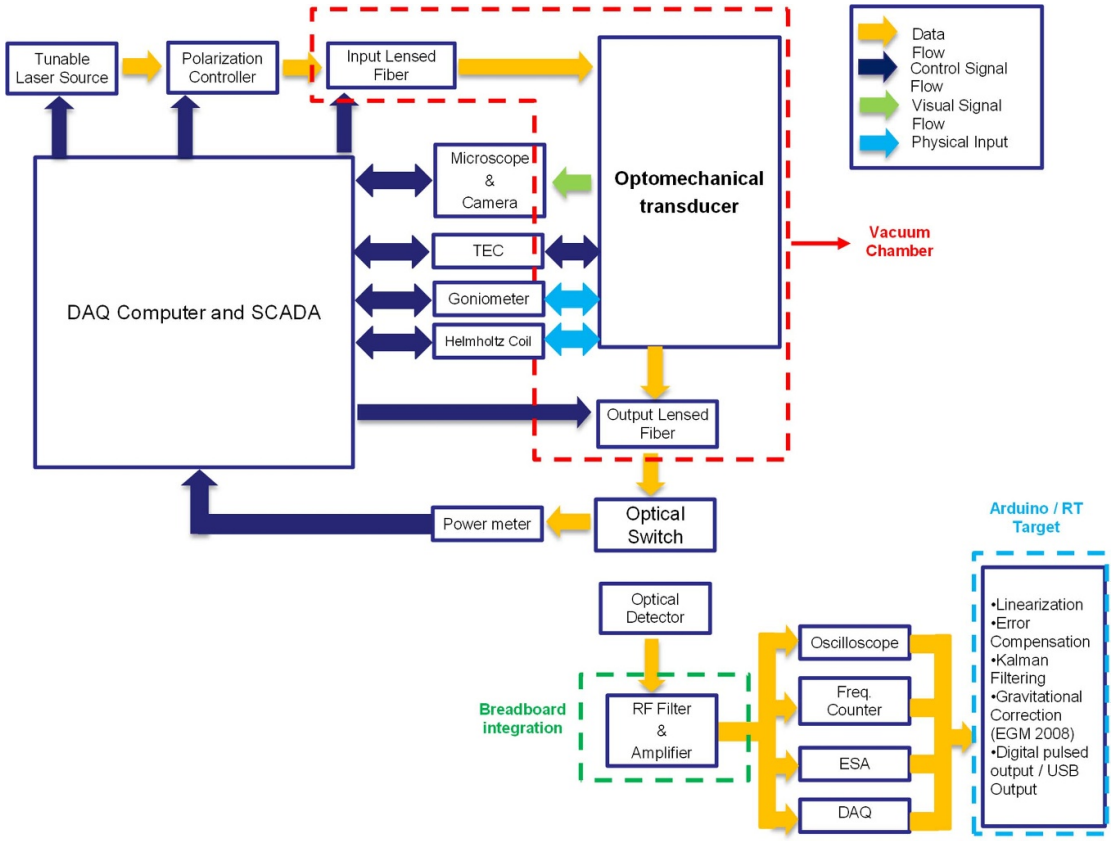

Figure 2. AtOMICS signal flow diagram. AtOMICS is controlled by our in-house software that integrates multiple hardware components with control algorithms for coupling automation, supervision, and testing. Control signals are sent to the different components connected via universal serial bus (USB). Visual feedback is obtained from the CCD camera on top of the microscope, which is moved to different regions of the setup during the coupling and testing processes. The output signal is monitored by the power meter to provide feedback and optimized fiber position. Multiple data acquisition devices can be connected and managed by the system depending on the type of test that is being performed.

are later analyzed and transmitted to other hardware, such as a real-time target, for further integration with other testing systems.

2.2. Software and coupling algorithms

The main characteristics of AtOMICS and the code that controls the system are presented in figure 3. AtOMICS can be assessed from a custom graphical user interface (GUI), as presented in figure 3(b). Here the controllers for some of the hardware functions are shown; they can be used to manually tune the equipment or to run the automated algorithms for coupling of the lensed optical fibers to the chiplets' edges. The interface continuously images and records the interior of the vacuum chamber, as captured by the CCD (charge-coupled device) camera and the microscope. The object detection algorithm is run over the video and detects the objects present in the images. Position information is kept and fed to the coupling algorithms, and the bounding boxes on the fibers and couplers are displayed to monitor the process.

In addition, the program constantly measures the pressure inside the chamber as well as the optical power on the output detector through the optical switch, which can direct 95% of the optical power to the optical detector or power meter as needed. AtOMICS constantly records this information every few seconds so that it can be correlated with experimental data. Moreover, the program indicates the status of the system hardware and keeps track of the microscope controller's encoder reading and the piezoelectric system's virtual encoder.

In order to design the coupling algorithms, the first step was the characterization of the input and output lensed fibers power profile when the system is coupled to a testing chiplet. The following data recorded with AtOMICS corresponds to the testing of a silicon photonics optomechanical chipset fabricated on SOI with a top silicon membrane thickness of 250 nm, as described in [36]. The optomechanical chiplet used is shown in figure 1(c), with the input optical fiber to the left. The optical fiber used is an anti-reflective (AR) coated lensed fiber with a 2 μm spot diameter and a nominal working distance of 12 μm that has been metalized a few mm from its tip. This optical fiber has been optimized to match the size of the coupler's mode and has been reinforced for inertial measurement applications similar to the ones described in [2]. The lensed optical

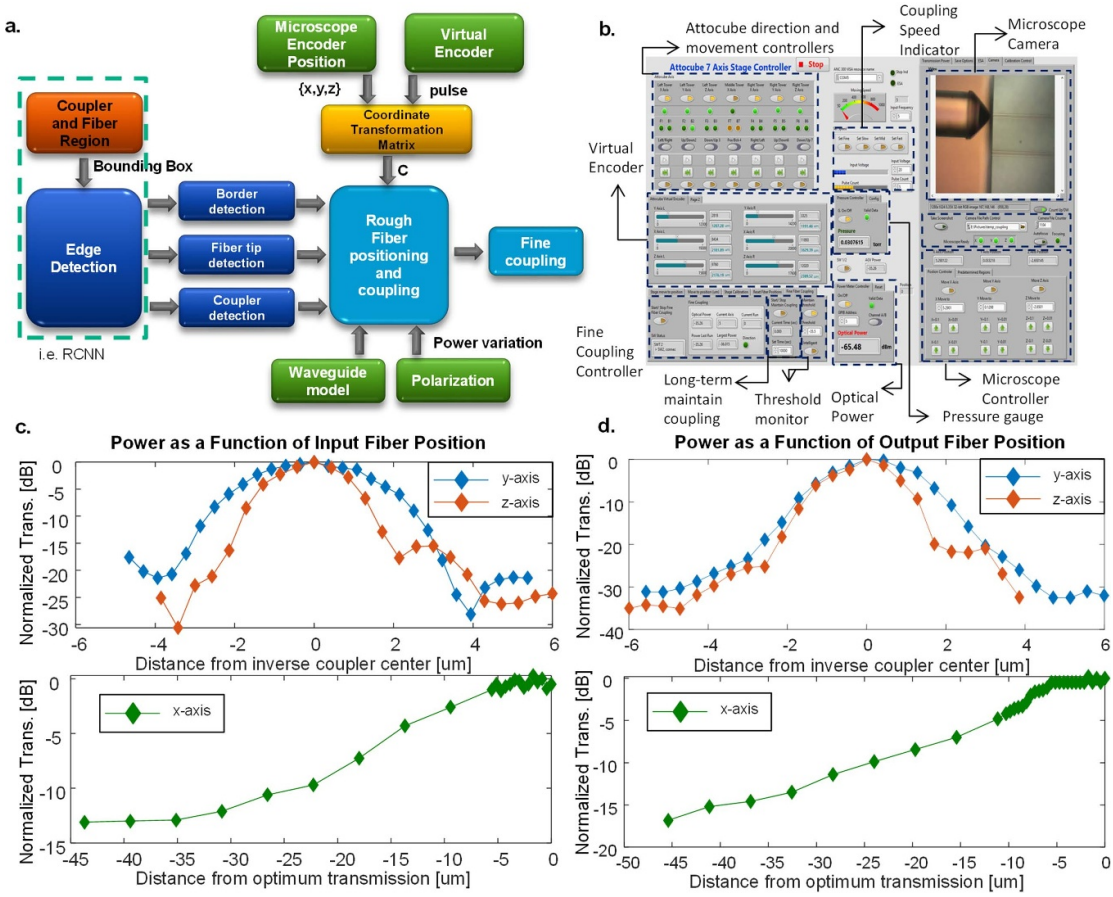

Figure 3. AtOMICS software and coupling system. (a), AtOMICS coupling algorithm. The system combines the computer vision model using data taken from the camera and the virtual encoder from the microscope position, to couple the lensed optical fiber to the edges of the chiplet. (b), graphical user interface (GUI) of AtOMICS. The system controls each degree-of-freedom from the optical fiber stages separately and provides multiple movement options as well as speeds. The coupling power and pressure are also continuously displayed on screen and recorded for further analysis. The microscope and camera can be controlled in parallel when the system is coupling the optical fiber actively. The encoder positions read from the microscope are displayed for the current and future movements. Additional controllers are present for auto-coupling, active alignment, and long-term coupling. (c), Transmitted power as a function of the lensed fiber position for the input side. Top figure shows the normalized transmission for the z-axis (up and down, orthogonal to the chiplet plane), and for the y-axis (north and south direction relative to the coupler in the plane parallel to the chiplet). Lower plot shows the transmission for the x-axis positioning, with negative distance defined as the fiber is going away from the chiplet. (d), Transmitted power as a function of the lensed fiber position for the output side. Top figure shows the normalized transmission for the y- and z-axis, and the bottom figure shows the x-axis.

fiber is positioned at the chiplet edge, and an optical waveguide travels across the chiplet from the coupler to the transducer; a second waveguide collects the optical signal from the transducer and propagates to the exit coupler. This optomechanical transducer has optical and mechanical modes that can be excited by using a driving laser. That light delivered to the transducer is confined in a slot cavity in the photonic crystal at the core of the structure; the electric field is confined in a subwavelength cavity, resulting in an electromagnetic gradient-induced optomechanical force that drives mechanical movements on a suspended structure [2, 37, 38]. The movement of this mechanical structure can be measured by the output detector as modulations in the optical carrier. The power dependence on the measured modes can be calculated and is described in [39, 40].

The input and output optical fiber power transmission profile as a function of position centered on the inverse tapered coupler is shown in figures 3(c) and (d). The z-axis is defined as out-of-plane and orthogonal to the chiplet plane, the y-axis runs north and south along and parallel to the chiplet edge, and the x-axis is aligned left and right along the waveguide and coupler axes. As shown in the upper plots of figures 3(c) and (d), the z-axis is, in general, the most sensitive axis, having a 15 dB transmission loss over a change in position $\Delta z \approx 2$ μm. This is followed by the y-axis with a 4 dB transmission loss over a change in position $\Delta y \approx 2$ μm. The x-axis is, in general, the least sensitive of the three as long as the fiber tip is maintained within 5 μm from the nominal fiber working distance after the device has been coupled. The working distance for the lensed optical fiber in this experiment is $\approx$12 μm. From the plots, it can also be seen that the transmitted power is, in general, more sensitive to the output fiber position than the input fiber position.

Table 1. Object detection algorithm performance. Mean average precision (mAP) and detection speed of multiple state-of-the-art object detection neural networks. *Indicates performance measured on the Microsoft COCO dataset; other performance is reported on the PASCAL VOC 2007 dataset. Further information can also be found in [43, 44].

Object detection network algorithm	mAP	Frames per second
SS + R-CNN [45]	66.0	0.03
SS + SPP-Net [46]	63.1	0.44
Fast R-CNN [47]	66.9	0.5
Faster R-CNN (VGG16) [48]	69.9	5
Faster R-CNN (ResNet101) [49]	76.4	5
YOLOv2 [50]	76.8	67
SSD512 [51]	74.3	59
FPN [52]	36.20*	5
Mask R-CNN [53]	35.7*	5

The reason for this lies in the physics of the optomechanical transducer more than in the waveguide/coupler system since input power accumulates inside the slot cavity on the center of the photonic crystal, and only a small part of the optical power is coupled back to the output waveguide. Once the transmission power profile and tolerances have been characterized, these values were fed into the coupling system as part of the coupling algorithm designed and described in figure 3(a).

The process of coupling the input and output lensed fibers to the on-chip waveguides is performed in two steps and illustrated in figure 3(a). First, a rough coupling step is performed by a computer vision algorithm that determines the location of the chiplets and the fibers, after which the system moves the fibers to the appropriate position. As shown in table 1, multiple state-of-the-art object detection neural networks were considered to determine the computer vision algorithm to be implemented. These algorithms are usually evaluated by the mean average precision (mAP) of the detections, as well as the speed at which the images can be processed. In order to pick the object detection algorithm, we based our decision on published performance metrics available on the PASCAL VOC 2007/12 [41] and Microsoft COCO [42] datasets. For our current application, the need for image processing speed, in frames per second (fps), is not as critical during the coupling process since the fibers are slowly moved across the setup; in contrast, precision is a high concern since errors in position detection could cause damage in fibers and couplers. For the current implementation, we decided to exchange speed for an increase in precision by going with an algorithm of the region-based convolutional neural networks (R-CNN) family which on average has the highest mAP, as shown in table 1. The chosen algorithm is based on the Faster R-CNN implementation, which runs at 5 fps, and is sufficiently fast for our application. The performance of Faster R-CNN has been measured at 76.4 on the PASCAL VOC 2007, which is very good for a core algorithm. However, the comparison table is used only as a general guideline, as final performance is dependent on various other systemic and implementation factors. In addition, we present the performance of other algorithms on the Microsoft COCO dataset as a comparison. Special attention is taken on Mask R-CNN, which is an algorithm that extends Faster R-CNN and could be used for semantic segmentation as a future implementation that can add an extra layer of accuracy for the solution of the presented detection and localization problem.

A second design choice made for the object detection algorithm is the convolutional backbone for image classification. A survey of convolutional networks that were considered is shown on table 2. In principle, the R-CNN family can use multiple backbones as long as the convolutional features can be shared between the region proposal and classification networks, which requires access to some intermediate layers. Another criterion that can be used is the number of parameters that each of these networks require, as this would impact performance and memory requirements.

In order to solve the object detection problem, we created a dataset containing ≈7300 images divided into multiple classes including lensed optical fiber and couplers. A first training step was performed on the classification networks using these set and initial weights trained on the Imagenet dataset, as is customary. The use of this dataset enables transfer learning from the ImageNet dataset which contains 14 million images annotated over 20 000 categories in order to help improve the model as low-level features and filters learned from this set can be extended to the classification problem at hand. By performing small tuning of the networks, we obtained the accuracy presented in column 4 of table 2. Good results were obtained with Xception and ResNet with 0.876 and 0.870 accuracy respectively on the testing set. With this information and our choice of the Faster R-CNN model, we decided to use a ResNet50 for the convolutional backbone. This network was implemented with 3×3 convolutional filters, where a pooling layer was placed after the initial filter layer, and is composed of a total of 50 layers. For the deeper layers, down sampling is performed, and as the feature map size is halved, the number of filters is doubled in order to maintain feature complexity [49].

Table 2. Classification networks performance. Multiple classification networks were tested as core of the R-CNN based object detector. The number of parameters used by each convolutional network architecture as well as of the box performance on the Imagenet and the customized set are reported.

Classification network type	# Parameters	Imagenet dataset accuracy	Optical fiber dataset accuracy
Xception [54]	22 855 952	0.790	0.876
VGGNET [55]	134 000 000	0.719	0.845
ResNet50 [56]	26 000 000	0.785	0.870
InceptionV3 [57]	24 000 000	0.788	0.827
InceptionResNetV2 [58]	56 000 000	0.801	0.848
1.0 MobileNet-224 [59]	3300 000	0.833	0.792
NASNetMobile [60]	89 000 000	0.827	0.774
EfficientNetB7 [61]	66 000 000	0.843	0.844
EfficientNetB3 [61]	12 000 000	0.816	0.845

Additional techniques such as image augmentation and early stopping have been used during the training process in order to prevent overfitting to the training and validation sets. Due to the complexity of the problem at hand, image detection algorithms do not use a sole metric to measure performance of the system, but one that combines multiple of them. While we have monitored loss and recall for the detection headers, as shown in table 2, and we have monitored similar metrics such as class loss and box loss of the region proposal, as well as the Mask R-CNN sections, for the segmentation and object detection problem at hand, we used mean Average Precision (mAP). This metric combines Intersection over Union (IoU), precision, and recall. It is based on the calculation of IoU over the predicted bounding box of the object that has been detected and the ground-truth from the labeled box. After training the object detection model in our custom dataset, we obtained a mAP of 55.2%.

The computer used for training the model, including the classification head and segmentation modules is one of the servers at the Wong's Lab at UCLA, which includes a set of two Intel Xeon E5 CPUs with 28 cores, 56 logical processors, and 128 GB of RAM. The model ran on an NVIDIA TITAN RTX GPU using Turing architecture, 130 Tensor TFLOPs of performance, 576 tensor cores, and 24 GB of GDDR6 memory. The total training time was ∼14 h.

As shown by figure 3(a), once the object detection algorithm outputs the regions where the lensed fibers and couplers are detected, their positions are marked. This information is used by the edge detector algorithm to further refine the limits of the object borders. The output is a point that represents the tip of the fiber as well as the center of the coupler.

In order to move the fiber to the initial position after the CNN image detection, the system checks the microscope encoders as well as the piezoelectric actuators' virtual encoders, and uses the chip border to calculate a coordinate transformation matrix $C_{\mathrm{M}}^{\mathrm{P}}$ used to reference the measurements from the microscope reference plane (M) to the piezoelectric actuators' reference frame (P). Next, the fiber is moved close to the coupler, and the measured power is monitored and mapped, creating a 3D power map as the fiber is moved close to the chiplet. In order to avoid possible local minima or power reflection from an input fiber that is positioned higher than the chiplet, the system uses the power models measured from figures 3(c) and (d). Once the fiber is positioned and the power meter has detected laser transmission, there is first a small optimization step, where the coupling is confirmed using the automated polarization controller and by checking that the power measured is, in fact, dependent on polarization. This rough coupling step is followed by a fine coupling step, where the program optimizes the power from both the input and output optical fibers, and the system is ready for data acquisition. A more detailed view of the coupling algorithm can be seen in figure 4, where a high-level Unified Modeling Language (UML) diagram of the calls that the main coupling monitor module makes to the other modules in AtOMICS is presented.

2.3. AtOMICS system performance

Figures 5(a)–(d) show some examples of images taken with AtOMICS during regular program operation. As shown, the couplers and the optical fibers have been positioned close together, inside the system's field-of-view, and the image detection algorithm has run. The two lensed optical fibers are now correctly detected and they can be positioned to be coupled by setting the correct option for calibration. After the different components have been detected, the next step is shown in figures 5(e) and (f), where the edge detection algorithm has been run for further position refinement.

For the current tests, AtOMICs has been run on an Intel Core i7 processor with 64 Gb of RAM, in our setup computer at the Wong's Lab in UCLA. The Mask R-CNN model used has a size of 256 Mb, and the classification head is around 92 Mb. The other modules of the AtOMICS system are lighter and use less than

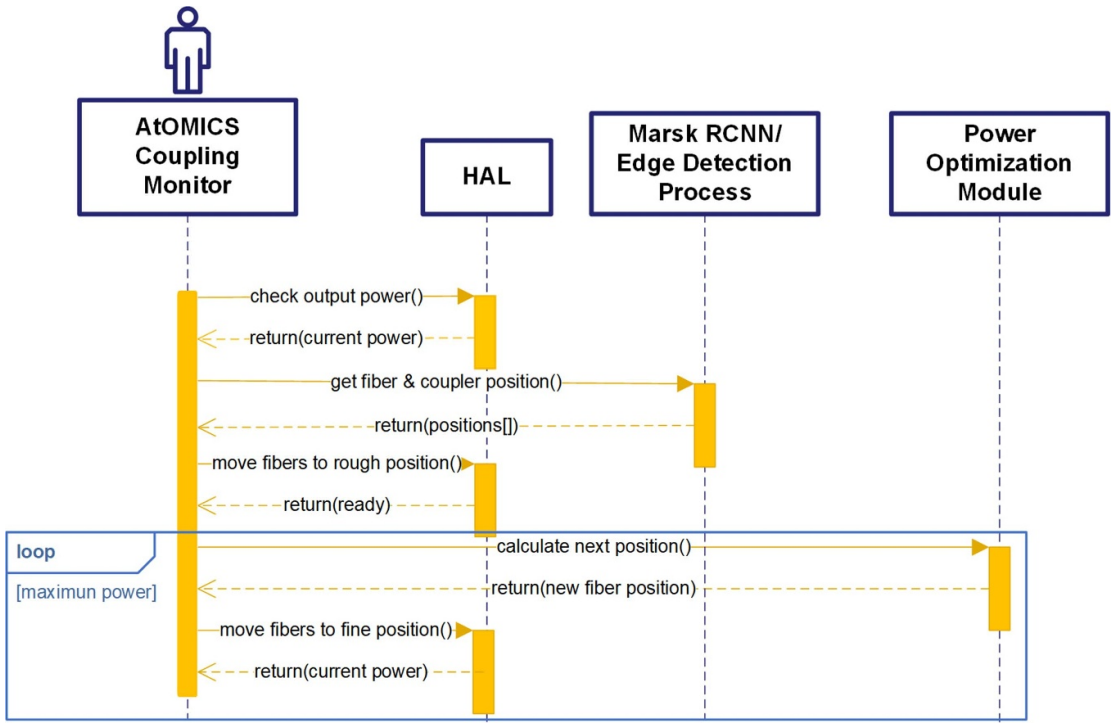

Figure 4. AtOMICS coupling algorithm. At the core of AtOMICS is the coupling monitor module, which decides the timing for different actions and coordinates the low and upper-level drivers. The system uses the hardware abstraction layer (HAL) as an interface to the optical detectors and the piezo electric stages that move the input and output optical fibers. Once the data from the HAL is processed, the system can decide if the object detection algorithm needs to be run, and if the contours of the objects need to be recalculated, to determine the accurate position of the components to be tested. This information is used to locate the optical fibers close to the edge coupler of the transducer to be tested. These steps constitute the rough coupling section. Once the position is confirmed, and the HAL can provide optical intensity data, the power optimization module is run, and used to refine the position of the optical fibers. This constitutes the fine coupling step, and is repeated until the maximum possible power has been achieved.

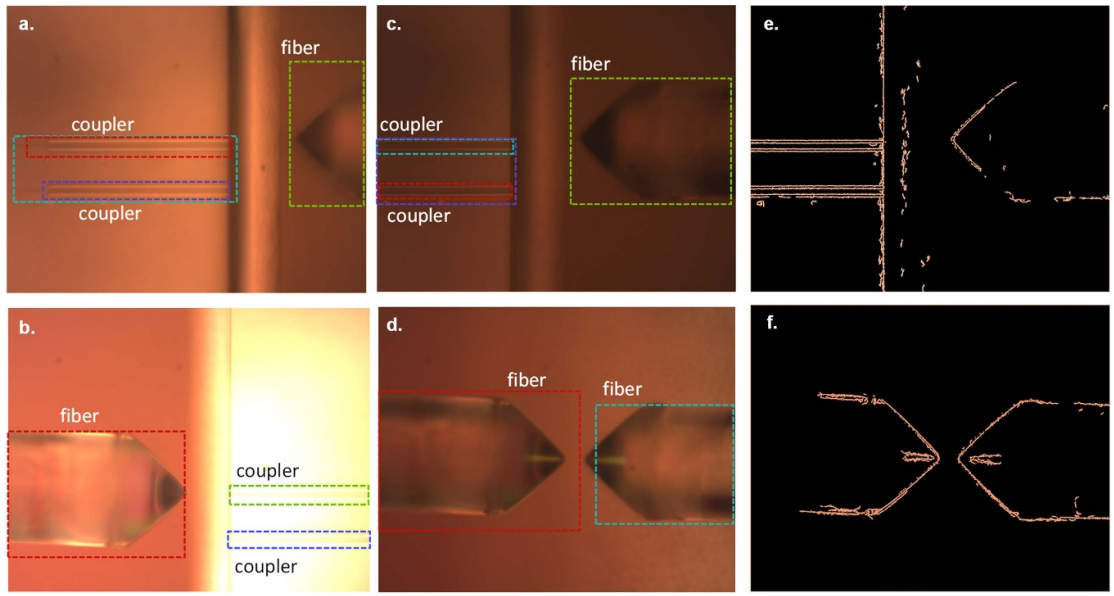

Figure 5. AtOMICS lensed fiber and inverse tapered couplers detection. (a)–(d) Images taken during the operation of the system. The system uses the camera and the object detection convolutional neural network (CNN) to locate the lensed fibers as well as the couplers in the images. The system can detect multiple occurrences of a similar object inside the frame. (e) and (f), edge detection inside the different regions. The coordinates of the fiber tip and the chip couplers, as well as the edge of the chiplets are calculated and sent as input to the system to plan the movements.

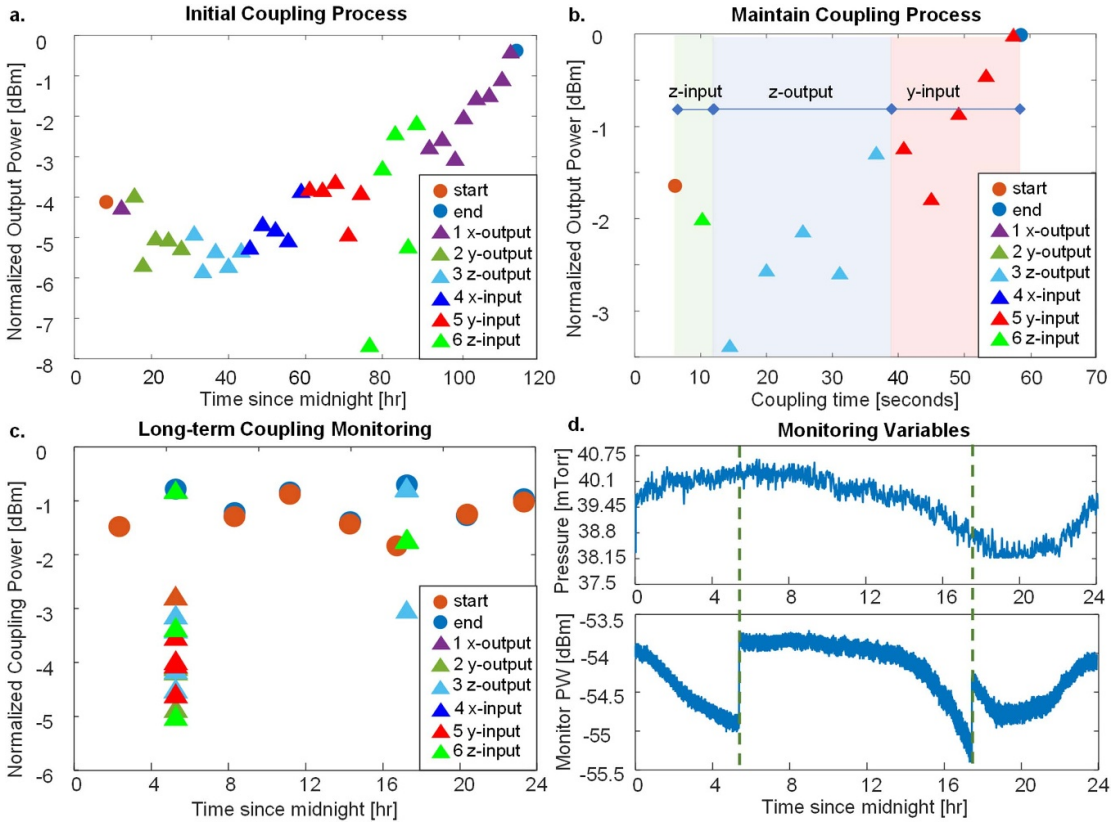

Figure 6. AtOMICS initial and long-term coupling. (a) Coupling process for fine-tuning. After light is detected and the polarization dependence has been confirmed, the system starts to optimize the coupling power. A sequence of movements is performed by both piezoelectric towers to position the optical fibers in an optimal position relative to the inverse couplers. A movement sequence example is shown for a process that takes around 110 s to converge. (b) Example of coupling process maintained. Once the system has been coupled, AtOMICS can maintain coupling for extended periods of time depending on the testing. Some actions can be configured so that the program can adjust to the experiment being performed and does not interpret a sudden loss of power due to experimental conditions changing, as a decoupling event. The trace shows a small example where the system has been told to recouple when power is below −31.5 dBm and stop when the recovered power is −31 dBm. Recovering in this example takes around 50 s. (c) Long-term coupling monitoring and power conservation in-between a set threshold. The figure shows AtOMICS running for a 24 h period. Events are shown where the system takes control of the experiment to monitor the total transmitted power from the optical switch. Two coupling intervention events are seen performed by the system. The first event requires multiple movements, but the second is completed with only three. (d) Figure shows the monitored power and the recorded pressure inside the system for a 24 h period during an experiment. A 2 mTorr pressure shift is recorded for a 24 h period, and the power monitored is also recorded. A change in power that occurs at ≈5 and ≈17.5 h can be seen, which eventually requires intervention from the program. Data in the figure corresponds with the piezoelectric movements performed in part (c).

200 Mb of RAM. Even though the presented Mask R-CNN model can have a frame rate of up to 5 fps, as detailed in table 1, the needed frame rate for this application is lower, at around 0.2 fps, as the movements of the piezo electric stages take around 2–5 s, and the position of the fiber does not need faster actualizations.

The operation of AtOMICS can be seen in figure 6, where panel *a* shows a sample fine-tuning coupling process in which the system optimizes the transmission by moving the different actuators from both the output and input lensed fibers in sequence. In this example, the different axes are marked by different colors, and the system moves them in sequence, optimizing the position of the fiber. After each movement is performed, the system checks the optical power transmission and averages it over a few measurements in order to get a stable reading. The time to take a reading, in this case, is ≈3 s, and the total coupling time is 108 s.

AtOMICS can also operate in power *monitor* mode in order to maintain the coupling on the optical fibers for extended data acquisition times. Figure 6(b) shows an example of a recoupling process where the lower power threshold has been set at −1.5 dBm, and the system is expected to couple back to 0 dBm. As shown, the system triggers at around 5 s and moves the *z*-axis of the input fiber (right fiber in figure 1(b)). Since this (represented by the bright green upright triangle) produces a decrease in power, it continues with the *z*-axis on the output side (left fiber in figure 1(b)). The system finalizes the series of movements with the *y*-axis of the input fiber, where the required coupling power is obtained. Subsequent motions such as the output fiber *y*-axis, input *x*-axis, and output *x*-axis are not needed, and thus the system exits the coupling

mode to continue monitoring the stability of the test silicon photonics transducer. The total recovery time is around 55 s.

An example of a longer transmission monitoring case is presented in figures 6(c) and (d). The presented data corresponds to a 24 h period where the program is configured to monitor the transmission power output from the device and recouple it if necessary. In addition, it takes back full control to monitor the full power every 3 h. The corresponding recorded pressure and monitored power data are presented in figure 6(d). As shown in the upper subpanel of this figure, the pressure during a one-day time period is cyclical, and the peak-to-peak variation corresponds to ≈2 mTorr. The lower subpanel shows the monitored power by the system, which corresponds to only a fraction of the total power since most of it goes to the optical detector through the switch. From time $t = 0$ h., the monitored power decreases by ≈2 dB until slightly after $t = 5.3$ h., wherein the system retakes control and recouples the system (the corresponding sequence of movements performed is noted in figure 6(c)). After the system is recoupled, the monitor power is constant for the next 10 h, where the system only does minor checks. After ≈10 h, power starts to decrease, which is an event that could have been triggered by a matching change in chamber pressure as noted in the upper panel. Again, AtOMICS takes control of the system and recouples above the programmed threshold. Continuous coupling and long-term power stabilization have been obtained. Further experiments have tested the performance of the system across time spans in the order of months with successfully maintained and stabilized fiber-chip-fiber coupling results.

3. Conclusion

In this work we present an Automated Optomechanical Intelligent Coupling System suitable for testing of silicon photonic chiplets that uses edge coupling through lensed optical fibers. The system uses a variation of the Faster R-CNN object detection architecture combined with post-processing algorithms in order to determine the position of the different elements and track them as they move them across the testing setup for automated and optimized laser chip coupling. The system is capable of precision fiber-to-chip alignment automatically and maintaining the alignment for time spans in the order of months tested. This system can aid in the self-testing and screening of silicon photonics devices in production and in applications where active, long-term alignment is required.

Data availability statement

All data that support the findings of this study are included within the article (and any supplementary files).

Acknowledgment

We acknowledge discussions with Wenting Wang, Noah Himed, Yongjun Huang, Li-Hsu Yang and Jiagui Wu. The authors acknowledge the edge coupler test samples from the Institute of Microelectronics, with Dim-Lee Kwong, Patrick Guo-Qiang Lo, and Mingbin Yu. The authors acknowledge support from NASA and JPL through the Small Spacecraft Technology Program (SSTP).

Conflict of interest

The authors declare no conflict of interest.

ORCID iDs

Connor Nasseraddin https://orcid.org/0009-0002-0688-8728
Talha Yerebakan https://orcid.org/0009-0007-8667-7651
Chee Wei Wong https://orcid.org/0000-0001-7652-7720

References

[1] Li Y L and Barker P F 2018 Characterization and testing of a micr-g whispering gallery mode optomechanical accelerometer *J. Lightwave Technol.* **36** 3919
[2] Huang Y, Flor Flores J G, Li Y, Wang W, Wang D, Goldberg N, Zheng J and Wong C W 2020 A chip-scale oscillation-mode optomechanical inertial sensor near the thermodynamical limits *Laser Photon. Rev.* **14** 1800329
[3] Flor Flores J G, Wang W, Huang Y, Wu J, Yerebakan T, Bai Q and Wong C W 2020 Low-frequency noise stabilization in optomechanical inertial accelerometers for high-resolution sensing *Conf. on Lasers and Electro-Optics (CLEO)* (*San Jose, CA*)
[4] Steglich P, Siegfried B, Mai C, Paul M, Weller M and Mai A M 2020 CMOS-compatible silicon photonic sensor for refractive index sensing using local back-side release *IEEE Photonics Technol. Lett.* **32** 1241

[5] Luan E, Shoman H, Ratner D, Cheung K and Chrostowski L 2018 Silicon photonic biosensors using label-free detection *Sensors* **18** 3519
[6] Adcock J, Bao J, Chi Y C X, Bacco D, Gong Q, Oxenløwe L, Wang J and Ding Y 2020 Advances in silicon quantum photonics *IEEE J. Sel. Top. Quantum Electron.* **27** 24
[7] Chang K-C, Cheng X, Can Sarihan M, Kumar A, Lee Y S, Zhong T, Gong Y, Xie J H, Shapiro F and Wong C W 2021 648 Hilbert-space dimensionality in a biphoton frequency comb: entanglement of formation and Schmidt mode decomposition *npj Quantum Inf.* **7** 11
[8] Gonzalez-Zalba M, De Franceschi S, Charbon E, Meunier T, Vinet M and Dzurak A 2021 Scaling silicon-based quantum computing using CMOS technology *Nat. Electron.* **4** 872
[9] Xue X *et al* 2021 CMOS-based cryogenic control of silicon quantum circuits *Nature* **593** 7858
[10] Wu J *et al* 2017 Mesoscopic chaos mediated by Drude electron-hole plasma in silicon optomechanical oscillators *Nat. Commun.* **8** 15570
[11] Luo C, Flor Flores J G, Shi B, Yu M, Lo G, Kwong D-L, Wu J and Wong C W 2019 Gb/s physical random bits through mesoscopic chaos in integrated silicon optomechanical cavities *Conf. on Lasers and Electro-Optics (CLEO)* (*San Jose, CA*)
[12] Wu J, Flor Flores J G, Yu M, Lo G, Kwong D-L, Duan S and Wong C W 2018 Chaos synchronization over 50 kilometers using monolithic silicon optomechanical cavities *Conf. on Lasers and Electro-Optics (CLEO)* (*San Jose, CA*)
[13] De Marinis L, Cococcioni M, Castoldi P and Andriolli N 2019 Photonic neural networks: a survey *IEEE Access* **7** 175827
[14] Steinbrecher G, Olson J, Englund D and Carolan J 2019 Quantum optical neural networks *npj Quantum Inf.* **5** 60
[15] Siew S Y *et al* 2021 Review of silicon photonics technology and platform development *J. Lightwave Technol.* **39** 4374
[16] Rickman A 2014 The commercialization of silicon photonics *Nat. Photon.* **8** 579
[17] Rakowski M, Meagher C, Nummy K and Aboketaf A 2020 45nm CMOS-silicon photonics monolithic technology (45CLO) for next-generation, low power and high speed optical interconnects *Optical Fiber Communication Conf.* (*San Diego, CA*)
[18] Carpenter L, Begovic A, Timalsina Y, Antohe A, Dikshit A, Baiocco C, Leake G, Fahrenkopf N and Harame D 2022 Low losses in an active silicon photonic multi-project wafer runs *Proc. SPIE* **12006** 1200602
[19] Lujan A 2018 Comparison of package-on-package technologies utilizing flip chip and fan-out wafer level packaging *Electronic Components and Technology Conf.* (IEEE)
[20] Sperling E 2020 Test costs spiking *Semiconductor Engineering, Test, Measurement & Analytics*
[21] Carroll L *et al* 2016 Photonic packaging: transforming silicon photonic integrated circuits into photonic devices *Appl. Sci.* **6** 426
[22] Dangel R, Hofrichter J, Horst F, Jubin D, La Porta A, Meier N, Soganci I, Weiss J and Offrein B 2015 Polymer waveguides for electro-optical integration in data centers and high-performance computers *Opt. Express* **23** 4736
[23] Song J, Harendra F, Roycroft B, Corbett B and Peters F 2009 Practical design of lensed fibers for semiconductor laser packaging using laser welding technique *J. Lightwave Technol.* **27** 1533
[24] Papes M *et al* 2016 Fiber-chip edge coupler with large mode size for silicon photonic wire waveguides *Opt. Express* **24** 5026
[25] He A, Guo X, Wang K, Zhang Y and Su Y 2020 Low loss, large bandwidth fiber-chip edge couplers based on silicon-on-insulator platform *J. Lightwave Technol.* **38** 4780
[26] Polster R, Yuan Dai L, Jimenez O, Cheng Q, Lipson M and Bergman K 2018 Wafer-scale high-density edge coupling for high throughput testing of silicon photonics *Optical Fiber Communications Conf. and Exposition (OFC)* (*San Diego, CA*)
[27] Cheben P, Halir R, Schmid J, Atwater H and Smith D 2018 Subwavelength integrated photonics *Nature* **560** 565
[28] Halir R, Ortega-Monux A, Benedikovic D, Mashanovich G, Wangüemert-Pérez J, Schmid J, Molina-Fernandez I and Cheben P 2018 Subwavelength-grating metamaterial structures for silicon photonic devices *IEEE Proc.* **106** 2144
[29] Yermakov O, Zeisberger M, Schneidewind H, Kim J, Bogdanov A, Kivshar Y and Schmidt M 2023 Advanced fiber in-coupling through nanoprinted axially symmetric structures *Appl. Phys. Rev.* **10** 011401
[30] Thomson D, Zilkie A, Bowers J, Komljenovic T, Reed G T, Vivien L, Marris-Morini D, Cassan E, Virot L and Fédéli J-M 2016 Roadmap on silicon photonics *J. Opt.* **18** 073003
[31] Romero-Garcia S, Marzban B, Merget F, Shen B and Witzens J 2013 Edge couplers with relaxed alignment tolerance for pick-and-place hybrid integration of III–V lasers with SOI waveguides *IEEE J. Sel. Top. Quantum Electron.* **20** 369
[32] Mu X, Wu S, Cheng L and Fu H Y 2020 Edge couplers in silicon photonic integrated circuits: a review *Appl. Sci.* **10** 1538
[33] Israil M, Anwar S A and Abdullah M Z 2013 Automatic detection of micro-crack in solar wafers and cells: a review *Trans. Inst. Meas. Control* **35** 606
[34] Rahman A A and Mousavi A 2020 A review and analysis of automatic optical inspection and quality monitoring methods in electronics industry *IEEE Access* **8** 183192
[35] De Coster J, De Heyn P, Pantouvaki M, Snyder B, Chen H, Mirinissen E, Absil P, Van Campenhout J and Bolt B 2016 Test-station for flexible semi-automatic wafer-level silicon photonics testing *IEEE European Test Symp. (ETS)* (*Amsterdam*)
[36] Flor Flores J, Yerebakan T, Wang W, Yu M, Kwong D, Matsko A and Wong C 2023 Parametrically driven inertial sensing in chip-scale optomechanical cavities at the thermodynamical limits with extended dynamic range *Laser Photon. Rev.* **17** 2200827
[37] Zheng J *et al* 2013 Feedback and harmonic locking of slot-type optomechanical oscillators to external low-noise reference clocks *Appl. Phys. Lett.* **102** 141117
[38] Li Y, Zheng J, Gao J, Shu J, Aras M and Wong C W 2010 Design of dispersive optomechanical coupling and cooling in ultrahigh-Q/V slot-type photonic crystal cavities *Opt. Express* **18** 23844
[39] Flor Flores J G, Huang Y, Li L, Iaia V, Yu M, Knowng D-L and Wong C W 2017 Power-dependence of high-Q optomechanical oscillators: from pre-oscillation, to oscillation slope, to Drude-plasma *Conf. on Lasers and Electro-Optics (CLEO)* (*San Jose, CA*)
[40] Huang Y, Flor Flores J G, Cai Z, Wu J, Yu M, Kwong D-L, Wen G, Churchill L and Wong C W 2017 Controllable optomechanical coupling and Drude self-pulsation plasma locking in chip-scale optomechanical cavities *Opt. Express* **25** 6851
[41] Everingham M, VanGool L, Williams C K I, Winn J and Zisserman A *The PASCAL visual object classes challenge 2012 (VOC2012)* (available at: www.pascal-network.org/challenges/VOC/voc2012/workshop/index.html)
[42] Lin T Y, Maire M, Belongie S, Hays J, Perona P, Ramanan D, Dollár P and Zitnick L 2014 Microsoft COCO: common objects in context *European Conf. on Computer Vision* (*Zurich*)
[43] Jiao L, Zhang F, Liu F, Yang S, Li L, Feng Z and Qu R 2019 A survey of deep learning-based object detection *IEEE Access* **7** 128837
[44] Zaidi S S A, Samar M, Aslam A, Kanwal N, Asghar M and Lee B 2022 A survey of modern deep learning based object detection models *Digit. Signal Process.* **126** 103514
[45] Girshick R, Donahue J, Darrell T and Malik J 2014 Rich feature hierarchies for accurate object detection and semantic segmentation *Conf. on Computer Vision and Pattern Recognition,* (*Columbus, OH*) (IEEE)

[46] He K, Zhang X, Ren S and Sun J 2015 Spatial pyramid pooling in deep convolutional *IEEE Trans. Pattern Anal. Mach. Intell.* **37** 1904–16
[47] Girshick R 2015 Fast R-CNN *IEEE Int. Conf. on Computer Vision* (*Santiago*)
[48] Ren S, He K, Girshick R and Sun J 2016 Faster R-CNN: towards real-time object detection with region proposal networks (arXiv:1506.01497v3)
[49] He K, Zhang X, Ren S and Sun J 2016 Deep residual learning for image recognition *Conf. on Computer Vision and Pattern Recognition,* (*Las Vegas, NV*) (IEEE)
[50] Redmon J and Farhadi A 2017 YOLO9000: better, faster, stronger *Conf. on Computer Vision and Pattern Recognition,* (*Honolulu, HI*) (IEEE)
[51] Liu W, Anguelov D, Erhan D, Szegedy C, Reed S, Fu C-Y and Berg A C 2016 SSD: single shot MultiBox detector (arXiv:1512.02325v5)
[52] Zhao Y, Han R and Rao Y 2019 A new feature pyramid network for object detection *Int. Conf. on Virtual Reality and Intelligent Systems (ICVRIS)* (*Jishou*)
[53] He K, Gkioxari G, Dollar P and Girshick R 2017 Mask R-CNN *Int. Conf. on Computer Vision,* (*Venice*) (IEEE)
[54] Chollet F 2017 Xception: deep learning with depthwise separable convolutions (arXiv:1610.02357v3)
[55] Simonyan K and Zisserman A 2015 Very deep convolutional networks for large-scale image recognition (arXiv:1409.1556v6)
[56] Kaiming H, Xiangyu Z, Shaoqing R and Jian S 2015 Deep residual learning for image recognition (arXiv:1512.03385v1)
[57] Szegedy C, Vanhoucke V, Ioffe S and Shlens J 2016 Rethinking the Inception architecture for computer vision *Conf. on Computer Vision and Pattern Recognition,* (*Las Vegas, NV*) (IEEE)
[58] Szegedy C, Ioffe S and Vanhoucke V 2016 Inception-v4, inception-resnet and the impact of residual connections on learning (arXiv:1602.07261v2)
[59] Howard A G, Zhu M, Chen B, Kalenichenko D, Wang W, Weyand T, Andreetto M and Adam H 2017 MobileNets: efficient convolutional neural networks for mobile vision applications (arXiv:1704.04861v1)
[60] Zoph B, Vasudevan V, Shlens J and Le Q V 2018 Learning transferable architectures for scalable image recognition (arXiv:1707.07012v4)
[61] Tan M and Le Q V 2020 EfficientNet: rethinking model scaling for convolutional neural networks (arXiv:1905.11946v5)